

## Enhancing superconductivity of $Y_5Rh_6Sn_{18}$ by atomic disorder

A. Ślebarski<sup>1,2,\*</sup>, M. Fijałkowski<sup>1</sup>, P. Zajdel<sup>1</sup>, M. M. Maška<sup>3</sup>, J. Deniszczyk<sup>4</sup>, M. Zubko<sup>4</sup>, O. Pavlosiuk<sup>5</sup>,  
K. Sasmal<sup>6</sup> and M. B. Maple<sup>6</sup>

<sup>1</sup>*Institute of Physics, University of Silesia in Katowice, 75 Pułku Piechoty 1, 41-500 Chorzów, Poland*


<sup>2</sup>*Centre for Advanced Materials and Smart Structures, Polish Academy of Sciences, Okólna 2, 50-950 Wrocław, Poland*

<sup>3</sup>*Department of Theoretical Physics, Wrocław University of Science and Technology, Wybrzeże Wyspiańskiego 27, 50-370 Wrocław, Poland*

<sup>4</sup>*Institute of Materials Engineering, University of Silesia in Katowice, 75 Pułku Piechoty 1A, 41-500 Chorzów, Poland*

<sup>5</sup>*Institute of Low Temperature and Structure Research, Polish Academy of Sciences, P.O. Box 1410, 50-950 Wrocław, Poland*

<sup>6</sup>*Department of Physics, University of California, San Diego, 9500 Gilman Drive, La Jolla, California 92093, USA*

 (Received 15 May 2020; revised 1 July 2020; accepted 31 July 2020; published 20 August 2020)

We investigate the effect of enhancement of superconducting transition temperature  $T_c$  by nonmagnetic atom disorder in the filled skutterudite-related tetragonal  $Y_5Rh_6Sn_{18}$  compound doped with Ca. We documented experimentally that  $Y_5Rh_6Sn_{18}$  and its Ca-doped alloys are electronically inhomogeneous at the nanoscale, when Ca content is smaller than  $\sim 1.5$  in the  $Y_{5-x}Ca_xRh_6Sn_{18}$  system, while for  $x \geq 1.5$  much stronger chemical phase inhomogeneity is observed with an about 20% volume fraction of the second 3:4:13 cubic phase, which we interpret as a fluctuation of stoichiometry within the bulk sample. Then the enhancement of  $T_c$  vs  $x$  could be modeled by a mechanism proposed in recent theoretical reports for increasing the mean-field transition temperature  $T_c$  in the presence of nonmagnetic disorder. The increase in disorder with doping increases the sample inhomogeneity and causes a systematic increase in  $T_c$ , while for two-phase  $x \geq 1.5$  samples the critical temperature  $T_c^* \approx 2 \times T_c$  rapidly increases. Based on band structure calculations performed under pressure, we demonstrate how the change in density of states would affect  $T_c$  of  $Y_5Rh_6Sn_{18}$ . We obtained the Grüneisen parameter  $\gamma_G$  larger for the inhomogeneous phase with respect to  $\gamma_G$  of the bulk  $T_c$  phase and attribute the enhancement of  $T_c$  to larger stiffening of the *high-temperature*  $T_c^*$  phase.

DOI: [10.1103/PhysRevB.102.054514](https://doi.org/10.1103/PhysRevB.102.054514)

### I. INTRODUCTION

The interplay between disorder and superconductivity is a subtle and fascinating phenomenon in quantum many-body physics. Observations of an enhancement of the superconducting transition temperature  $T_c$  when the amount of disorder in a material is increased are particularly interesting. The mechanisms for enhancing  $T_c$  by nonmagnetic disorder depend on the nature of disorder. They have not been explained well enough, although the problem is intensively studied experimentally and theoretically. Disorder is most often associated with the presence of atomic-scale disorder and causes the enhancement of the scattering rate [1], e.g., by impurities (with amount  $x$ ), structural defects, or local inhomogeneity. Therefore, attention usually has been focused on measuring and explaining the change of  $T_c$  with the degree of disorder, e.g., expressed by  $x$ . The conventional BCS superconductors with isotropic superconducting  $s$ -wave gaps generally are not sensitive to dilute nonmagnetic impurities, while the presence of magnetic dopants, even with a small amount, can drastically reduce the critical temperature of their superconducting state [2–4]. According to the Anderson theory [5], magnetic impurities which break the time-reversal

symmetry substantially influence the properties of a conventional superconductor, while nonmagnetic impurities have a negligible effect. On the other hand, in the case of a strongly anisotropic gap,  $T_c$  should also be reduced by nonmagnetic impurities.

Novel strongly correlated superconductors (SCS) with the presence of a quantum critical point (QCP) have been known for the last decades [6,7]. In such critical regimes, the atomic disorder acting as a perturbation, regardless of how weak it may be, can be decisive and change the nature of the quantum macrostate. The perturbation leads to novel phenomena, like the disorder-enhanced superconductivity discovered in a series of SCSs. One can cite a number of experimental reports of disorder-enhanced  $T_c$  [8–14]; however, the mechanism of increasing  $T_c$  is still under debate. The interpretation of doping effects is not always straightforward; impurities may affect not only scattering rates but also other properties of the system, such as the shape of the Fermi surface or the magnetic properties away from impurities. Therefore it seems necessary to investigate not only the superconducting phase but also normal state to correctly interpret the influence of impurities on superconductivity. Our most recent studies focus on skutterudite-related  $R_3M_4Sn_{13}$ -type superconductors, where  $R = La, Y, \text{ or } Ca$ , and  $M = d$ -electron-type metals, which show strong enhancement of critical temperature  $T_c$  caused by disorder [13]. These *nonmagnetic* quasiskutterudites have been reported as  $s$ -wave BCS superconductors with

\* Author to whom correspondence should be addressed:  
andrzej.slebarski@us.edu.pl

the presence of atomic-scale disorder leading to the appearance of a *novel* superconducting state characterized by the critical temperature  $T_c^*$  higher than  $T_c$  of the bulk phase. Many experimental and theoretical attempts have been undertaken to answer the current question of why the superconducting transition temperature  $T_c$  increases when the amount of disorder is increased (e.g., Refs. [13,15]). Very recently Gastiasoro and Andersen [15] theoretically explained disorder-generated  $T_c$  enhancements for two separate scenarios: Dilute disorder in multiband superconductors and dense disorder in conventional one-band superconducting systems. The proposed mechanisms qualitatively model the superconducting properties of the strongly disordered  $Y_{5-x}Ca_xRh_6Sn_{18}$  alloys, both for small and larger concentrations of disorder. For several reasons the skutterudite-related  $Y_5Rh_6Sn_{18}$  parent superconductor is an interesting avenue [16] for continued research. It forms a single phase with tin vacancies. In the complex structure of  $Y_5Rh_6Sn_{18}$ , both the atomic displacements as well as the nonstoichiometry of different crystallographic sites can be treated as structural defects (cf. Ref. [17]) which determine the superconducting properties of the system. For the family of similar skutterudite-related compounds this atomic disorder is a cause of a structural second-order-type transition at temperature  $T^* \sim 350$  K [17,18] and related distinct anomalies and/or charge density wave (CDW) formation at much lower temperatures of  $\sim 160$  K. When  $Y_5Rh_6Sn_{18}$  is doped with Ca, one can control the increase of disorder and investigate its impact on the sample superconductivity. The further increase of doping leads to strong enhancement of sample inhomogeneity; for Ca content  $x > 1.25$  a significant increase in  $T_c$  is documented, which can be discussed within the models proposed in Ref. [15].

## II. EXPERIMENTAL AND COMPUTATIONAL DETAILS

The  $Y_{5-x}Ca_xRh_6Sn_{18}$  alloys were prepared by the arc-melting technique and then annealed at 870 °C for 2 weeks. All samples were examined by x-ray diffraction (XRD) analysis. The sample with  $x = 0$  was the subject of our previous report [16]. Patterns of samples with nonzero Ca content were collected on a PANalytical Empyrean diffractometer equipped with a Cu  $K\alpha_{1,2}$  source. Diffractograms were refined using the FULLPROF SUITE set of programs [19].

Stoichiometry and homogeneity were checked by the electron microprobe technique (scanning microscope JSM-5410). To obtain the surface images and structural properties of nanometer-size crystallites, the transmission electron microscopy (TEM) observations were performed using a JEOL high-resolution (HRTEM) JEM 3010 microscope operating at a 300-kV accelerating voltage and equipped with a Gatan  $2k \times 2k$  Orius 833SC200D CCD camera. The samples were crushed in the agate mortar and then the powder was suspended in isopropanol. The resulting material after dispersion in the ultrasonic bath was deposited on a Cu grid with an amorphous carbon film standardized for TEM observations. Selected area electron diffraction (SEAD) patterns and fast Fourier transform (FFT) patterns were indexed using dedicated ELDYF software [20].

Electrical resistivity  $\rho$  at ambient pressure and magnetic fields was investigated by a conventional four-point ac

technique using a PPMS (physical properties measurement system) device. Resistivity under pressure was measured in a piston-cylinder cell (Ref. [21] for details of the method).

Magnetic ac susceptibility was measured using the Quantum Design PPMS platform. The dc magnetic susceptibility and magnetization were carried out in the temperature range 1.8–400 K and in applied magnetic fields up to 7 T using a Quantum Design superconducting quantum interference device (SQUID) magnetometer.

The x-ray photoelectron spectroscopy (XPS) spectra were obtained with monochromatized Al  $K\alpha$  radiation at room temperature in the vacuum of  $6 \times 10^{-10}$  Torr using a PHI 5700 ESCA spectrometer. The samples were broken under high vacuum immediately before measuring the spectra.

The electronic structure under pressure was investigated for  $Y_5Rh_6Sn_{18}$  using the WIEN2K package [22], which employs the density functional theory (DFT)-based full-potential linearized augmented plane waves (FP-LAPW) method complemented with local orbitals (LO) [23]. The pressure was simulated by decrease/increase of the unit-cell volume with respect to that measured at room temperature. We used the Birch-Murnaghan isothermal equation of state [24] to estimate hypothetical applied pressure corresponding to systematic decreasing (sample under external pressure) or increasing (lattice expansion due to negative pressure, e.g., effect of hypothetical chemical pressure) of the unit-cell volume:  $V(P) = V(0)[1 + \frac{B_0}{B_0'}P]^{-1/B_0'}$ , where  $V(0)$  is the unit-cell volume experimentally obtained at room temperature and ambient pressure, while the bulk modulus  $B_0$  and its pressure derivative  $B_0'$  were calculated. The band structure calculations were performed for the paramagnetic system with the chemical formula  $(Sn_{1-x}Y_x)Y_4Rh_6Sn_{18}$  (tetragonal structure, space group  $I4_1/acd$ ), using the experimental lattice parameters and the positional parameters listed in Table I in Ref. [16]. The self-consistent DFT calculations were performed for the following situations:  $\Delta V/V(0) = -0.06$  ( $\equiv 7.02$  GPa),  $-0.04$  ( $\equiv 4.42$  GPa),  $-0.02$  ( $\equiv 2.09$  GPa), 0 (ambient pressure),  $+0.02$  ( $\equiv -1.87$  GPa), and  $+0.04$  ( $\equiv -3.55$  GPa). The set of LO and valence states (VB), respectively, is assumed as follows: Y –  $[4s^24p^6]_{LO}\{4d^15s^2\}_{VB}$ ; Rh –  $[4s^24p^6]_{LO}\{4d^85s^1\}_{VB}$ ; Sn –  $[4p^64d^{10}]_{LO}\{5s^25p^2\}_{VB}$ , and the scalar-relativistic Kohn-Sham was applied with spin-orbit coupling (SOC) accounted for by means of the second variational method [23]. We used the gradient approximation (GGA) form of the exchange-correlation energy functional, with parametrization (PBEsol) derived for solids by Perdew *et al.* [25]. For all atoms the muffin-tin radii ( $R_{MT}$ ) were assumed to be 0.127 nm. The values of parameters determining the accuracy of calculations were assumed as follows:  $l_{max} = 10$ ,  $G_{max} = 14$ , and  $K_{max} = 8.0/R_{MT} \simeq 0.175$  nm $^{-1}$ . The  $k$  mesh was tested against the total energy convergence, and satisfactory precision, of a few millielectronvolts, was achieved with a  $7 \times 7 \times 7$  mesh ( $N_k = 40\vec{k}$  vectors in an irreducible Brillouin zone, IBZ).

## III. RESULTS AND DISCUSSION

### A. $Y_{5-x}Ca_xRh_6Sn_{18}$ : Structural properties

Doping with Ca introduces a nontrivial evolution of structural parameters and phase contents. The primary structure

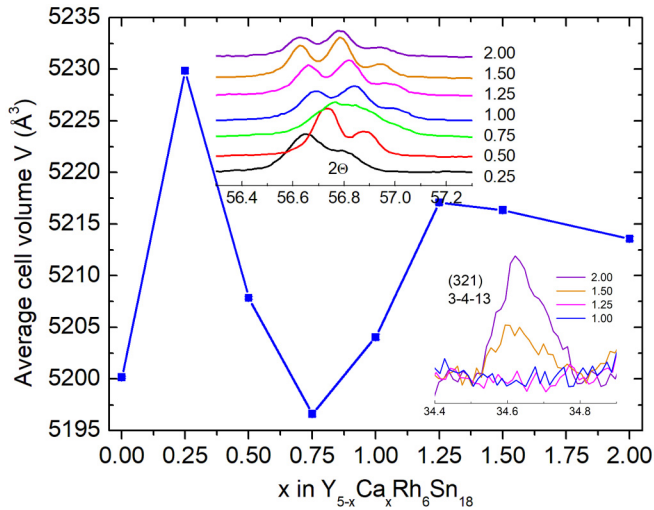


FIG. 1. Variation of an average tetragonal unit-cell volume of the 5:6:18 phase vs Ca content. The inset in the center presents an evolution of shape of four reflections (6 6 0), (8 2 4), (6 0 12), and (2 2 16) of the tetragonal 5:6:18 type phase. The inset in the right corner illustrates the appearance of the (3 2 1) reflection of the cubic (c) 3:4:13 type phase.

of each system is always based on a derivative of a 5:6:18 type tetragonal cell [16], the volume of which has been used as a reference ( $x = 0$ ) in Fig. 1. In the 0.25–0.50 Ca range, the primary structure is well described by the tetragonal cell symmetry, and the shape of peaks begins to drastically change at 0.75 Ca (see central inset in Fig. 1). The last sample seems to have a high level of disorder and small coherent domain size, which is seen from broad peak widths. Starting from 0.75 Ca, the main phase is no longer tetragonal and we refer to it as phase 1. However, it is closely related to 5:6:18 structure since the diffraction pattern is very similar with the exception of a weak peak splitting. Samples with nominal 1.00 and 1.25 Ca content are no longer tetragonal, but at the moment we cannot uniquely assign a space group to phase 1. The initial analysis indicates that the deformation is most likely monoclinic. Unfortunately, the size of the unit cell makes it almost impossible to solve the deformed structure from a powder pattern. However, in order to follow the structural trends with Ca content, we have used the fact that the deformation is weak and applied a rudimentary tetragonal approximation

TABLE I. The parameters obtained from structural, ac susceptibility and specific heat data for characterization of the  $Y_{5-x}Ca_xRh_6Sn_{18}$  superconductors. Electronic specific heat coefficient  $\gamma_0 \sim \text{DOS}(\epsilon_F) \equiv 2N(\epsilon_F)$  is obtained for  $T > T_c$  from the linear dependence of  $C/T$  against  $T^2$  at  $T = 0$  in zero magnetic field.  $\lambda$  and  $\lambda^*$  characterize the electron-phonon coupling strength for the  $T_c$  and  $T_c^*$  phases, respectively. Both parameters are obtained self-consistently from Eq. (12), which will be discussed. For phase 1 an approximate tetragonal cell is given.

$x$	Structure	Lattice parameters at RT (Å)	$T_c$ (K)	$T_c^*$ (K)	$\gamma_0 \pm 1.1$ (mJ/mol K <sup>2</sup> )	$\theta_D \pm 10$ (K)	$\lambda$	$\lambda^*$	$dH_{c2}/dT \pm 0.05$ (10 <sup>4</sup> × Oe/K)
0	$I4_1/acd$	$a = 13.7577(2), c = 27.4741(5)$	3.08	3.19	9.3	200	0.46	0.47	-1.72
0.25	$I4_1/acd$	$a = 13.7774(3), c = 27.5519(10)$	2.44	3.49	4.2	170	0.45	0.50	-1.75
0.5	$I4_1/acd$	$a = 13.7617(1), c = 27.4988(7)$	3.10	3.72	16.3	150	0.51	0.52	-1.88
0.75	Phase 1	$a = 13.7418(3), c = 27.5189(9)$	3.10	3.92	17.6	156	0.50	0.53	-1.95
1.0	Phase 1	$a = 13.7669(4), c = 27.4575(10)$	3.78	4.11	21.1	159	0.52	0.54	-1.85
1.25	Phase 1	$a = 13.7816(4), c = 27.4681(7)$	3.85	4.18	24.7	149	0.53	0.55	-1.88

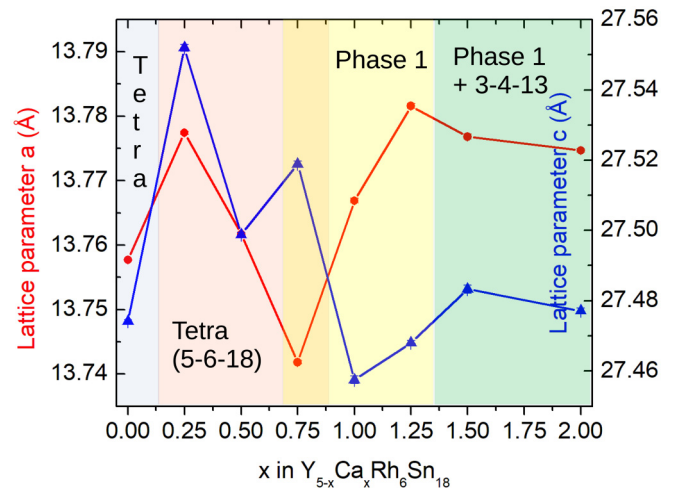


FIG. 2. Lattice parameters of an average tetragonal unit cell vs Ca content. Color shading marks regions with different phase contents. From the left: Clean tetragonal [16], tetragonal with Sn, border area with a larger atomic disorder and with a clear divergence between parameters  $a$  and  $c$ , phase 1 + Sn, phase 1 + Sn + cubic. The tetragonal cell symmetry begins to be observed for the sample  $x = 0.75$  (see the text).

to model the main phase in the remaining samples. The cell volume and cell parameters obtained this way are visualized in Figs. 1 and 2, and collected in Table I. Two compositions with the highest Ca content ( $x > 1.25$ ) have three phases: The main phase derived from the 5:6:18 system ( $>0.8$  mass fraction), a secondary phase based on a cubic 3:4:13 phase like  $Ca_3Rh_4Sn_{13}$  ( $\approx 0.05$ – $0.1$  mass fraction), which increases in quantity as seen from the increase of  $(321)_c$  reflection in the right inset in Fig. 1, and about 0.05 of Sn. A secondary phase ( $<0.01$ – $0.1$  mass fraction) present in samples can be identified as a tetragonal tin. The presence of tin whiskers is also clear from SEM micrographs (see Fig. 3), where they are separated from the bulk of the grain.

From the dependence of lattice parameters on Ca content (Fig. 1) one can state that phase 1 reaches the upper limit of Ca content at  $x = 1.25$ , when the excess of Ca separates in the Ca-rich cubic phase. This conclusion is corroborated by flattening of the average tetragonal lattice parameters  $a$  and  $c$ , which indicates that they are no longer sensitive to doping.

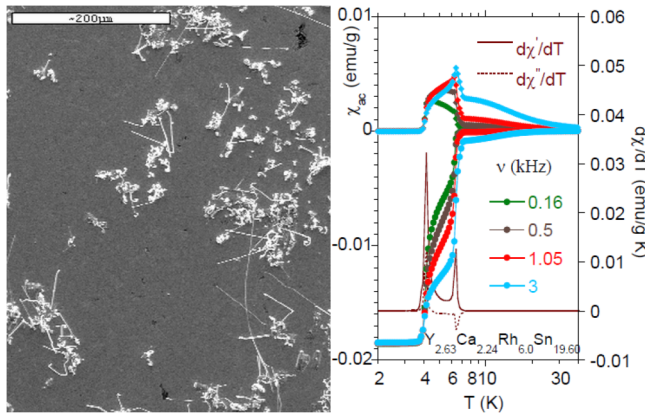


FIG. 3. Left panel shows SEM image of the surface topography obtained for the  $Y_{2.63}Ca_{2.24}Rh_{6.0}Sn_{19.60}$  sample with well-separated Sn whiskers. The dark surface fractions show the minority cubic 3:4:13  $Ca_3Rh_4Sn_{13}$ -like phase. The right panel shows the ac susceptibility and its derivatives  $d\chi_{ac}/dT$ . The respective maxima in  $d\chi_{ac}'/dT$  and  $d\chi_{ac}''/dT$  determine the critical temperature of the bulk  $T_c$  and inhomogeneous  $T_c^*$  phases, respectively, while  $\chi_{ac}(T)$  is frequency  $\nu$ -dependent and shows a broad transition which visualizes strongly inhomogeneous state with distribution of various superconducting gaps  $\Delta$ , well approximated by the function  $f(\Delta)$  (cf. Ref. [26]). Within the limit of high  $\nu$ ,  $\chi_{ac}'$  tends to exhibit the high-temperature  $T_c^*$  phase with a broad transition to full Meissner state.

Interestingly, the attempt to solve the structure of phase 1 from TEM selected area diffraction revealed an interesting feature of the material. In the XRD pattern, sharp peaks connected with both approximately tetragonal 5:6:18 and cubic 3:4:13 phases suggest that they are well crystallized, which usually indicates phase separation.

However, inspection of one of the images told a different story. Figure 4 shows results of the transmission electron microscopy investigations performed for the strongly inhomogeneous  $Y_{2.0}Ca_{2.0}Rh_{6.0}Sn_{17.3}$  sample. The left panel shows the selected powder particle in a bright-field image. The middle panel exhibits a high-resolution image of the crystallite grain. By the two red squares two regions of interests were indicated, each of them showing the components with different structures. Based on the performed fast Fourier transform (FFT) analysis the upper fragment displayed in the right panel can be indexed as a cubic structure with symmetry  $Pm\bar{3}n$  (the insert shows the indexation results). Respectively, the bottom region

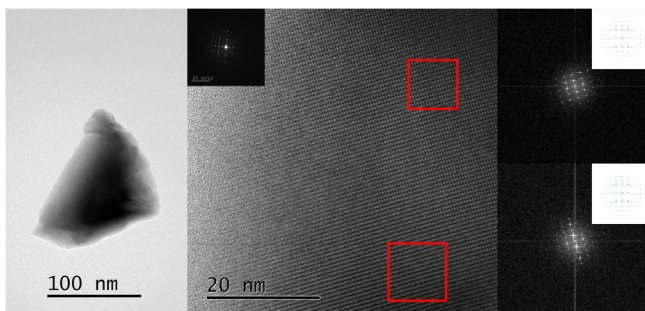


FIG. 4. TEM bright-field image of  $Y_{2.0}Ca_{2.0}Rh_{6.0}Sn_{17.3}$ .

can be identified as the surface fraction of the sample with tetragonal structure. The performed FFT pattern shown in the lower insert to the figure is well indexed within the tetragonal symmetry  $I4_1/acd$ . This fact indicated that in addition to a standard phase separation, the two related structures can smoothly blend into each other within one grain.

### B. The meaning of disorder in the system of $Y_{5-x}Ca_xRh_6Sn_{18}$ superconductors

The end points  $Y_5Rh_6Sn_{18}$  and  $Ca_5Rh_6Sn_{18}$ , like of the  $Y_{5-x}Ca_xRh_6Sn_{18}$  series, are not formed as isostructural compounds; thus it cannot be assumed that the systematic replacement of Y by Ca reflects continuously atomic disorder, which is measured by the function of Ca dopant concentration (see Figs. 1 and 2). On the other hand, the results of the XRD study justify considering the concept of “disorder” as a variable dependent on  $x$  that justifies explaining the size of the superconducting transition temperature depending on the degree of atomic disorder and quality of the sample.

Doping at a low concentration level, reflected by the smooth change of the lattice parameters and the volume of the unit cell as a function of the dopant concentration, here is considered as the elemental impurity effect and gives the basis for interpreting the increase in  $T_c$  at the level of the dilute disorder case (cf. Ref. [15]). However, the mixture of two phases remaining spatially separated from each other ( $x > 1.25$ ) is discussed as the effect of strong fluctuations in both atomic disorder and composition, which leads to a significant increase in the  $T_c$  value as a result of phase fluctuations (cf. Ref. [15]). The phase separation also reflects the application of the two-gap scenario developed as a mechanism for the specific heat-matching procedure, as well as the observation of two superconducting phase transition temperatures using both specific heat and magnetic susceptibility. The variety of “structural” properties of  $Y_{5-x}Ca_xRh_6Sn_{18}$  gives opportunity for discussion of different reasons for significant increasing of  $T_c$  within the one system, which seems to be useful for understanding the superconductivity of the real superconducting materials.

### C. $Y_{5-x}Ca_xRh_6Sn_{18}$ : Thermodynamic characterization

A comparative study has shown that disorder has a significant impact on  $T_c$ . Figure 5 compares the frequency dependence of the real ( $\chi'$ ) and imaginary ( $\chi''$ ) components of ac mass magnetic susceptibility  $\chi_{ac}$  and displays derivative  $d\chi'/dT$  and  $d\chi''/dT$  for the selected  $Y_{5-x}Ca_xRh_6Sn_{18}$  samples. The maxima in  $d\chi'/dT$  and  $d\chi''/dT$  we assigned, respectively, to critical temperatures  $T_c$  and  $T_c^*$ . The real ( $\chi'$ ) and imaginary ( $\chi''$ ) parts of  $\chi_{ac}$  shown in Fig. 5(a) display a broad transition between the normal and superconducting states of  $Y_5Rh_6Sn_{18}$ , which signals the presence of an inhomogeneous *high-temperature* superconducting  $T_c^*$  phase, well approximated by a simple Gaussian gap  $\Delta$  distribution (see Refs. [13,17]), while  $d\chi_{ac}/dT$  does not indicate the presence of the  $T_c$  bulk phase. This behavior can be explained by the fact that  $T_c^*$  and  $T_c$  are very similar ( $\Delta T_c = T_c^* - T_c = 0.1$  K) for  $Y_5Rh_6Sn_{18}$ . It looks different when the pristine sample is doped with Ca [in Fig. 5(b)]. Within the concentration range of  $0 < x \leq 1.25$ ,  $d\chi'/dT$  shows two narrow and well-separated maxima at  $T_c$  and at  $T_c^*$ . Moreover,

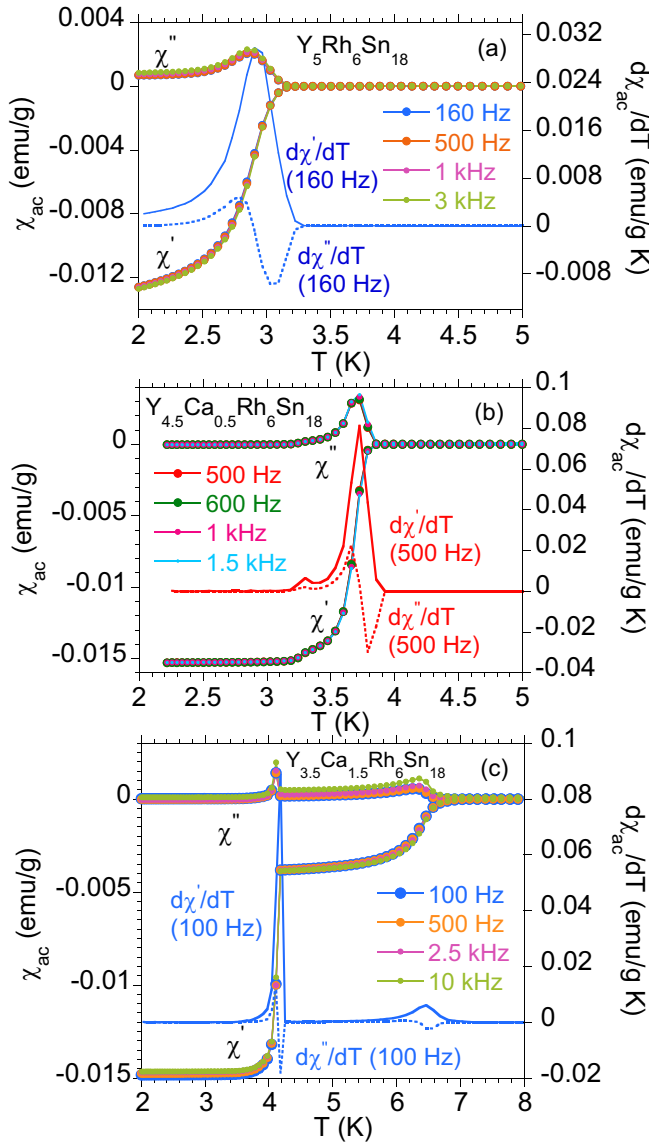


FIG. 5. Temperature dependencies of the real  $\chi'$  and imaginary  $\chi''$  components of the ac mass magnetic susceptibility for  $Y_{5-x}Ca_xRh_6Sn_{18}$ , measured at different frequencies  $\nu$  in the field with amplitude 2 Oe. Derivative  $d\chi'/dT$  and  $d\chi''/dT$  as a function of temperature are also shown. Panel (a) displays the data for pristine  $Y_5Rh_6Sn_{18}$  sample, panel (b) shows the data for  $Y_{4.5}Ca_{0.5}Rh_6Sn_{18}$ , panel (c) shows  $\chi_{ac}$  for a strongly inhomogeneous two-phase sample  $Y_{3.5}Ca_{1.5}Rh_6Sn_{18}$ . The frequency dependence of  $\chi_{ac}$  is detected only for the strongly inhomogeneous sample in panel (c).

perfect diamagnetism of the full Meissner state with the expected value of  $\chi' = -1/(4\pi d) \approx -0.011$  emu/g and mass density  $d$  is reached for these samples at temperatures  $T < T_c$ . In the case of two-phase samples [ $x > 1.25$ , panel (c)]  $\chi'$  shows the presence of about a 25% volume fraction of a minority phase  $T_c^*$ , while the full Meissner state is reached below  $T_c$ . For samples  $x \sim 2$ , the susceptibility  $\chi_{ac}$  shows a broad superconducting transition for the  $T_c^*$  phase (as shown in Fig. 3) as a result of the presence of inhomogeneous superconducting regions with various gaps  $\Delta$ , well approximated by the Gauss curve [26]. Figure 6 displays the heat

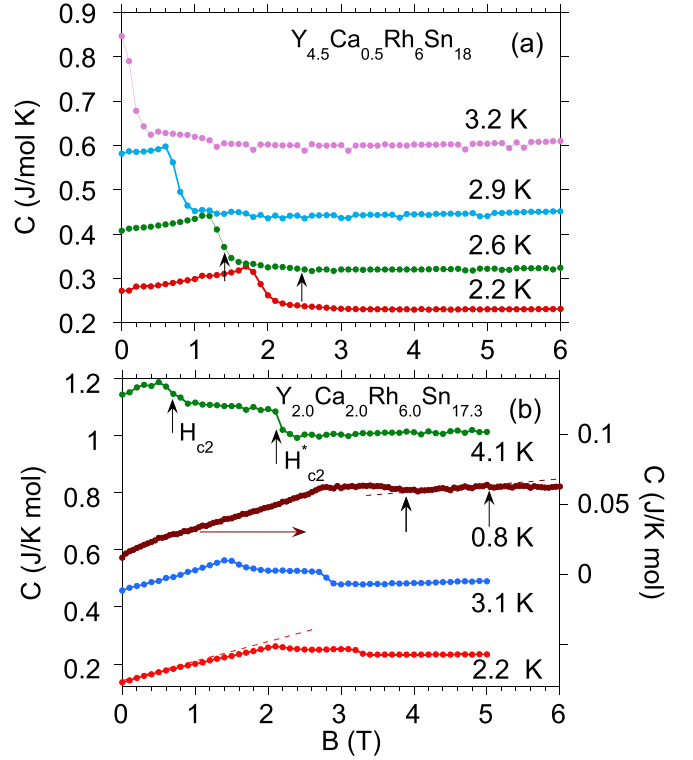


FIG. 6. Heat capacity  $C$  as a function of magnetic field  $B$  at constant temperature  $T$  for  $Y_{4.5}Ca_{0.5}Rh_6Sn_{18}$  (a) and two-phase sample  $Y_{2.0}Ca_{2.0}Rh_{6.0}Sn_{17.3}$  (b). The critical fields obtained for the bulk ( $T_c$ ) and *high-temperature* ( $T_c^*$ ) phases are labeled as  $H_{c2}$  and  $H_{c2}^*$ , respectively, and are indicated by arrows. The  $C$  isotherms show at the lowest temperatures nonlinear field dependence, which suggests two-band superconductivity. Similar behavior was observed for the series of  $Y_{5-x}Ca_xRh_6Sn_{18}$  compounds  $x \leq 1.25$ .

capacity isotherms  $C_T(B)$  measured vs magnetic field for the single-phase sample  $Y_{4.5}Ca_{0.5}Rh_6Sn_{18}$  [panel (a)] and for the two-phase sample  $Y_{2.0}Ca_{2.0}Rh_{6.0}Sn_{17.3}$  [panel (b)]. The  $C_T(B)$  isotherms shown in panel (a) exhibit a clear kink at the critical field  $H_{c2}$  for  $T < T_c$ , while at  $H_{c2}^* > H_{c2}$  the data display only some weak feature. This weakly visible feature is associated with the nanoscale disorder generated by doping of a  $Y_5Rh_6Sn_{18}$  superconductor with Ca, which leads to the appearance of a *new* inhomogeneous superconducting state, characterized by the critical temperature  $T_c^*$ , and is characteristic of a family of similar quasiskutterudite superconductors [13]. Similar  $C_T(B)$  isotherms were also measured for remaining compounds  $x \leq 1.25$ , while for the strongly inhomogeneous  $Y_{2.0}Ca_{2.0}Rh_{6.0}Sn_{17.3}$  sample the  $C_T(B)$  data shown in panel (b) exhibit a clear kink either at  $H_{c2}$  or  $H_{c2}^*$ . Figure 7 displays the specific heat shown as  $C(T)/T$  for  $Y_{4.5}Ca_{0.5}Rh_6Sn_{18}$  [panel (a)] and for a dirty two-phase sample  $Y_{2.0}Ca_{2.0}Rh_{6.0}Sn_{17.3}$  [panel (b)]. The specific heat of the bulk  $T_c$  phases shown in panels (a) and (b) can be well approximated by a two-gap model:

$$\frac{C(T)}{T} = \gamma' + \beta'T^2 + \frac{1}{T}A \left[ \eta \exp\left(-\frac{\Delta_1}{k_B T}\right) + (1 - \eta) \exp\left(-\frac{\Delta_2}{k_B T}\right) \right], \quad (1)$$

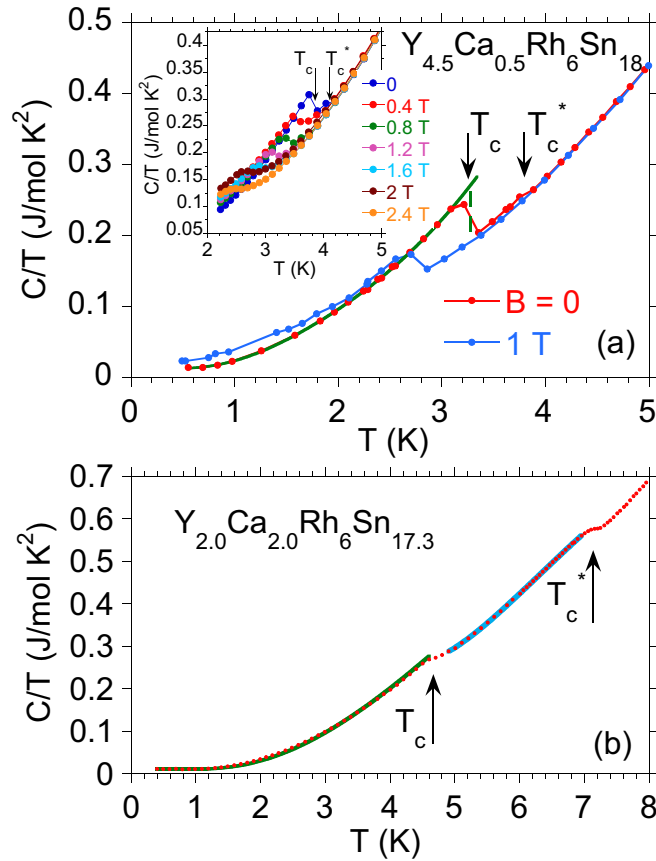


FIG. 7. (a) Temperature dependence of specific heat,  $C(T)/T$ , for  $Y_{4.5}Ca_{0.5}Rh_6Sn_{18}$ . The arrows indicate the bulk  $T_c$  phase and the *high-temperature*  $T_c^*$  phase, respectively. The green line is the best fit of Eq. (1) to the  $C(T)/T$  data in the temperature region  $T < T_c$  for  $\eta = 0.95$ ,  $\Delta_1/k_B = 17.8$  K,  $\Delta_2/k_B = 4.7$  K,  $\gamma = 0.009$  J/mol K<sup>2</sup>, and  $\beta = 0.0013$  J/mol K<sup>4</sup>. The inset displays the  $C(T)/T$  data at magnetic field  $B$  carried out for  $Y_{3.75}Ca_{1.25}Rh_6Sn_{18}$ . (b) For the  $Y_{2.0}Ca_{2.0}Rh_6Sn_{17.3}$  sample the  $C(T)/T$  data for  $T < T_c$  can also be approximated by the two-gap model [Eq. (1)] with the parameters  $\eta = 0.95$ ,  $\Delta_1/k_B = 11.0$  K,  $\Delta_2/k_B = 4.2$  K,  $\gamma_0 = 0.010$  J/mol K<sup>2</sup>, and  $\beta = 0.007$  J/mol K<sup>4</sup>. The *high-temperature*  $T_c^*$  phase in the temperature region  $T_c < T < T_c^*$  is well fitted (blue line) by the expression  $C(T)/T = \gamma' + \beta'T^2 + \frac{1}{T}A \exp[-\Delta(0)/k_B T]$  with  $\gamma' = 0.009$  J/mol K<sup>2</sup>,  $\beta' = 0.010$  J/mol K<sup>4</sup>, and  $\Delta(0)/k_B = 12.3$  K.

with the parameters listed in the description of Fig. 7. In the two-gap scenario, the electronic specific heat  $C(T)/T$  is considered to be a sum of two contributions with different superconducting gaps  $\Delta_1$  and  $\Delta_2$ . Such a behavior is expected from band structure calculations, which give various  $s$ ,  $p$ , and  $d$  electron states at the Fermi level. This is, however, not the case of the *high- $T_c^*$*  phase in panel (b), where the  $C(T)/T$  data are much better approximated by classical one-gap model. Figure 8 displays the zero-field electrical resistivity  $\rho$  for  $Y_{4.5}Ca_{0.5}Rh_6Sn_{18}$ , which exhibits a sharp transition between the normal and superconducting states. Similar  $\rho(T)$  data were obtained for the remaining  $Y_{5-x}Ca_xRh_6Sn_{18}$  samples with small content,  $x < 1.5$ , of Ca.

Parameters for characterization of the superconductivity of the  $Y_{5-x}Ca_xRh_6Sn_{18}$  alloys, determined from comprehensive

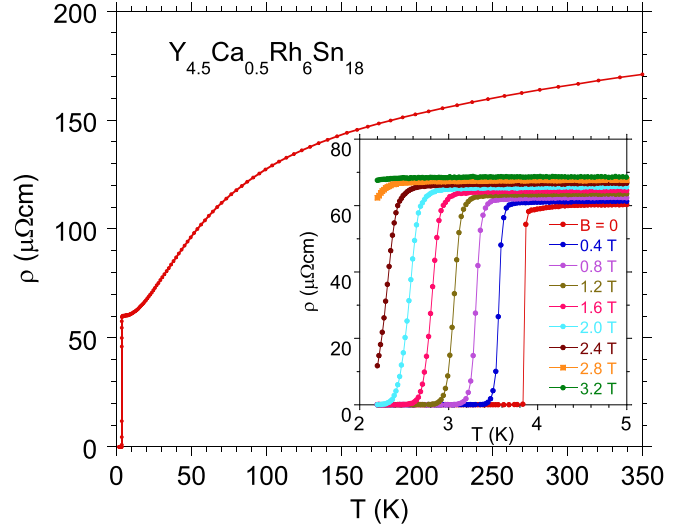


FIG. 8. Electrical resistivity  $\rho(T)$  for  $Y_{4.5}Ca_{0.5}Rh_6Sn_{18}$ . The inset shows  $\rho(T)$  at various externally applied fields.

measurements, are presented in Table I and will be used for modeling the superconductivity.

#### D. Superconductivity of $Y_{5-x}Ca_xRh_6Sn_{18}$ in the presence of atomic disorder

The temperature dependence of  $H_{c2}$  in dirty superconductors, i.e., superconductors where the coherence length  $\xi$  is larger than the mean-free path, is normally explained with the Werthamer–Helfand–Hohenberg (WHH) [27,28] or Maki–de Gennes [29] theories. The WHH theory predicts a linear temperature dependence of  $H_{c2}$  near  $T_c$ ,

$$H_{c2}(0) = -0.69T_c \left. \frac{dH_{c2}}{dT} \right|_{T=T_c}, \quad (2)$$

which agrees with the data shown in Fig. 9 for the series of  $Y_{5-x}Ca_xRh_6Sn_{18}$  samples ( $0 < x \leq 1.25$ ) and for a two-phase  $Y_{2.0}Ca_{2.0}Rh_6Sn_{17.3}$  sample. However, WHH does not predict the positive curvature of  $H_{c2}(T)$  close to  $T_c^*$  for parent  $Y_5Rh_6Sn_{18}$  compound. Moreover, for the experimental  $\frac{dH_{c2}}{dT}$  relations near the critical temperature, WHH expects critical fields  $H_{c2}(0)$  smaller by about 1 T than the actual values shown in Fig. 9. This means that for each case shown in Fig. 9, WHH theory is not good enough for describing the  $H - T$  dependencies. Very recently we have proposed a two-band model for more accurately describing the  $H - T$  data for  $Y_5Rh_6Sn_{18}$  [16].  $Y_5Rh_6Sn_{18}$  was classified as a dirty superconductor with the coherence lengths  $\xi_{GL}(0) \approx 9$  nm, larger than the mean-free path  $l \approx 6$  nm. The  $\xi_{GL}(0)$  and  $l$  BCS parameters were obtained in the framework of Ginzburg-Landau-Abrikosov-Gorkov (GLAC) theory of the type-II superconductors [27]. The  $Y_{5-x}Ca_xRh_6Sn_{18}$  compounds  $0 < x \leq 1.25$  are found to be superconductors close to the dirty limit and have  $\xi_{GL}(0) < l$ . For example, the parameters calculated for  $Y_{4.5}Ca_{0.5}Rh_6Sn_{18}$  are in the following relation: Electronic mean-free path  $l(0) = 1.27 \times 10^4 [\rho_n(n^{2/3}S/S_F)]^{-1} = 84$  nm and  $\xi_{GL} = 8$  nm

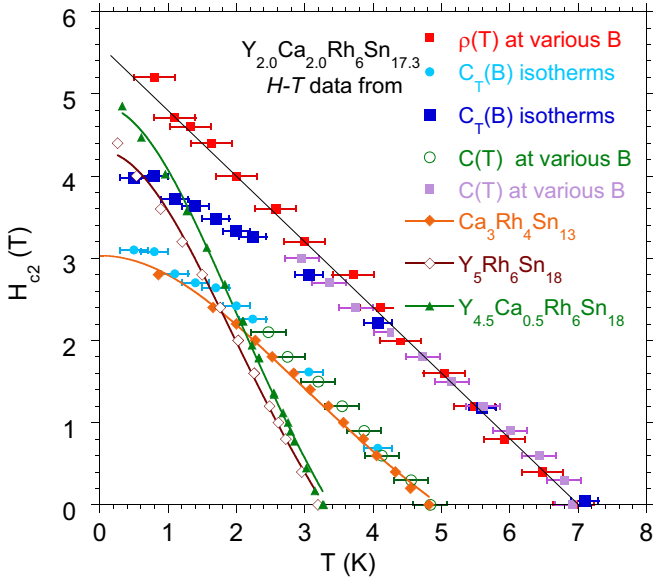


FIG. 9. Temperature dependence of the upper critical field  $H_{c2}$  in the  $H - T$  phase diagram for two-phase sample  $Y_{2.0}Ca_{2.0}Rh_{6.0}Sn_{17.3}$ . The points on the  $H - T$  plane are determined from specific heat  $C_B(T)$  and/or  $C_T(B)$  data and from resistivity  $\rho_B(T)$  measurements, respectively, for the two phases. An error due to blurring of the transition is shown too. The squares represent the data assigned to the  $Y_5Rh_6Sn_{18}$ -type phase doped by Ca (of about 80% of sample volume), while open circles describe the second phase of  $Ca_3Rh_4Sn_{13}$ -type doped with Y. The figure also shows the  $H - T$  plots for  $Y_5Rh_6Sn_{18}$  [16] (brown open diamonds) and for  $Ca_3Rh_4Sn_{13}$  [31] (yellow filled diamonds) reference parent compounds, respectively, for comparison, which are approximated by the Ginzburg-Landau (GL) model:  $H_{c2}(T) = H_{c2}(0)\frac{1-t^2}{1+t^2}$ , and  $t = T/T_c$ . The  $H - T$  data for  $Y_{4.5}Ca_{0.5}Rh_6Sn_{18}$  (green filled diamonds) with GL fit are also shown.

[Eq. (3), Ref. [30]],

$$\xi_{GL} = \left[ 2.90 \times 10^{32} (T_c \gamma_0)^2 \left( n^{2/3} \frac{S}{S_F} \right)^{-2} + 1.60 \times 10^{12} \rho_n \gamma_0 T_c \right]^{-1/2} [R(\lambda_{tr})]^{1/2} (1-t)^{-1/2}. \quad (3)$$

To calculate  $l$  and  $\xi_{GL}(0)$  we used experimental data:  $\rho_n = 60 \times 10^{-6} \Omega \text{ cm}$  is the normal-state resistivity approximated to  $T = 0$ , the electronic specific heat coefficient in the superconducting state  $\gamma_0 = 596 \text{ erg/cm}^3 \text{ K}^2$ ,  $n$  is the density of conduction electrons in  $\text{cm}^{-3}$ ,  $S/S_F$  is the ratio of the Fermi surface area to the Fermi surface of the free electron gas,  $S_F = 4\pi(3\pi^2 n)^{2/3}$ , and  $R(\lambda_{tr})$  is the Gorkov function of order unity [ $R(0) = 1$ ,  $R(\infty) = 1.17$  [30]]. Equation (4) allows one to estimate the value of  $n^{2/3} \frac{S}{S_F} = 2.5 \times 10^{13} \text{ cm}^{-2}$ ,

$$\left. \frac{dH_{c2}}{dT} \right|_{T=T_c} = \left[ 9.55 \times 10^{24} \gamma_0^2 T_c \left( n^{2/3} \frac{S}{S_F} \right)^{-2} + 5.26 \times 10^4 \gamma_0 \rho_n \right] [R(\lambda_{tr})]^{-1}, \quad (4)$$

for  $\left. \frac{dH_{c2}}{dT} \right|_{T_c} = -1.88 \times 10^4 \text{ Gs/K}$  (in Fig. 9), taking  $R(\lambda_{tr}) = 1$ , when  $\lambda_{tr} = 5.51 \times 10^{-21} \rho_n (n^{2/3} S/S_F) (\gamma_0 T_c)^{-1} \sim 10^{-14}$  is negligibly small. One of the reasons why the WHH theory does not describe the  $H - T$  dependencies for  $Y_{5-x}Ca_xRh_6Sn_{18}$  is that these superconductors do not obey the condition of the dirty limit  $\xi > l$ . There are also other reasons for deviation of the experimental data from the WHH curve, e.g., a strong-coupling effect can increase  $H_{c2}(0)$  (this effect, however, is reduced in the case of disordered superconductors [32]), or  $H_{c2}(T)$  can be affected by the presence of two bands (the case of  $Y_5Rh_6Sn_{18}$ , see Ref. [16]). Also, the specific heat data and complex electronic structure at the Fermi level suggest that  $H_{c2}(T)$  behavior can be affected by the presence of two bands. We calculated the critical fields from the theory of Gurevich [33], which is obtained by adapting the Eilenberger and Usadel equations to the case of a two-band dirty superconductor. The reduced magnetic field, defined as  $h = H_{c2} D_1 / 2 \Phi_0 T$ , is given by the following nonlinear equation:

$$a_0 [\ln t + U(h)] [\ln t + U(\eta h)] + a_2 [\ln t + U(\eta h)] + a_1 [\ln t + U(h)] = 0, \quad (5)$$

where  $U(x) \equiv \psi(x + 1/2) - \psi(1/2)$ ,  $\psi(\dots)$  is the digamma function,  $D_1$  is the band diffusivity, and  $\eta = D_2/D_1$ . The parameters  $a_{0,1,2}$  can be expressed by the intra- and interband BCS superconducting coupling constants  $\lambda_{11}$ ,  $\lambda_{22}$ ,  $\lambda_{12}$ , and  $\lambda_{21}$ . Figure 10 shows that the predictions of the two-band WHH theory better agree with the experimental data for the series of  $Y_{5-x}Ca_xRh_6Sn_{18}$  compounds with Ca content  $x < 2$  than the standard one-band theory. The agreement is better both at low temperature, where the two-band approach predicts higher values of the critical field, and at high and intermediate temperature, where it gives a relatively wide range of temperatures with a linear dependence  $H_{c2}(T)$ . It does not concern the bulk  $T_c$  superconducting phase of  $Y_{2.0}Ca_{2.0}Rh_{6.0}Sn_{17.3}$  and  $Ca_3Rh_4Sn_{13}$ , which both are well fitted by the one-band WHH approach.

### E. Band structure of $Y_5Rh_6Sn_{18}$ under pressure, the impact of pressure on an inhomogeneous superconducting state, phenomenology

The electronic structure of  $Y_5Rh_6Sn_{18}$  has been recently analyzed in detail [16], and now we present *ab initio* calculations under pressure. Figure 11 compares the valence-band photoelectron spectroscopy (VB XPS) spectra for  $Y_5Rh_6Sn_{18}$  with the calculated bands under pressure. The ground state was calculated as *nonmagnetic* under the wide range of external pressure. We used the Birch-Murnaghan isothermal equation of state [24],

$$P(V) = \frac{3B_0}{2} \left[ \left( \frac{V_0}{V} \right)^{\frac{7}{3}} - \left( \frac{V_0}{V} \right)^{\frac{5}{3}} \right] \times \left\{ 1 + \frac{3}{4} (B'_0 - 4) \left[ \left( \frac{V_0}{V} \right)^{\frac{2}{3}} - 1 \right] \right\}, \quad (6)$$

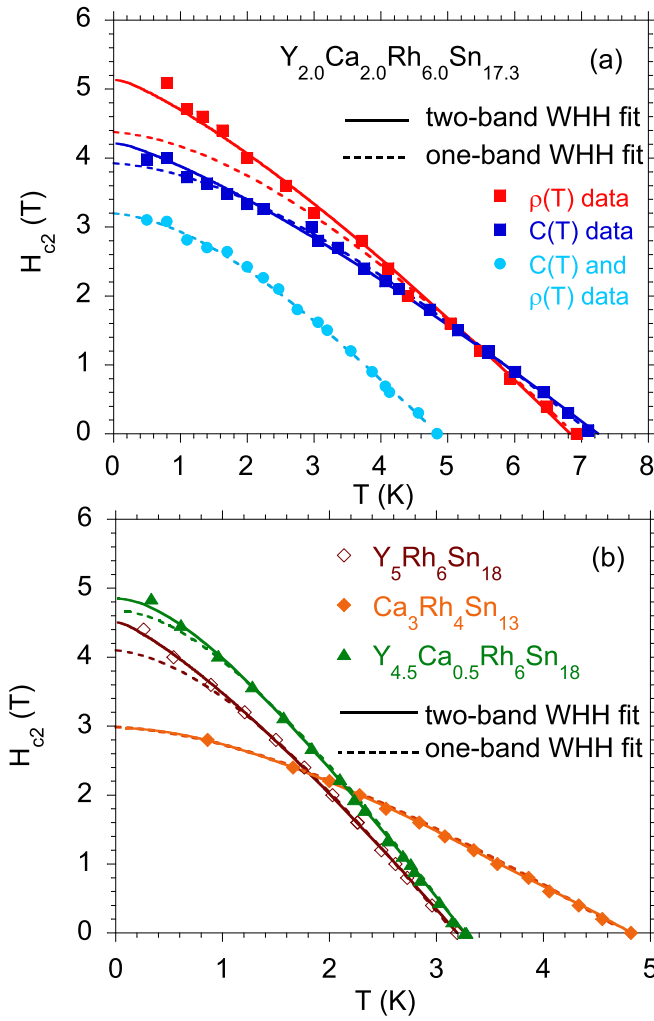


FIG. 10. The upper critical field  $H_{c2}$  for  $Y_{2.0}Ca_{2.0}Rh_{6.0}Sn_{17.3}$  [panel (a)] and for  $Y_5Rh_6Sn_{18}$ ,  $Ca_3Rh_4Sn_{13}$ , and  $Y_{4.5}Ca_{0.5}Rh_6Sn_{18}$  [panel (b)] approximated by the one-band (dotted lines) and two-band (solid lines) WHH model on the base of Gurevich theory [33] [Eq. (5)]. The points on the  $H - T$  diagram illustrate identical  $H_{c2}(T)$  relationships, such as those shown in Fig. 9, similarly the colors were assigned to the same superconductors, respectively.

to compute the volume depending on the pressure, where the bulk modulus  $B_0 = -V(\frac{\partial P}{\partial V})_T = 98.70$  GPa and its pressure derivative  $B'_0 = (\frac{\partial B_0}{\partial P})_T = 4.42$ . A comparison of the calculated and experimental bands shows that the total density of states reflects all of the features found in the VB XPS spectra of  $Y_5Rh_6Sn_{18}$ . The main peak at  $\sim 3$  eV originates mainly from the Rh  $4d$  states, while the electronic valence bands located at about 7 eV are dominated by Sn  $5s$  states (for details see [16]). Our *ab initio* calculations documented the linear scaling of  $DOS(\epsilon_F)$  with  $P$  in the region of  $0 < P < 4.5$  GPa, giving the change  $\frac{dDOS(\epsilon_F)}{dP} = 0.6$  1/(eV f.u. GPa). The calculated DOSs shown in Figs. 11 and 12 move with  $P$  towards a larger bare value of binding energy with respect to  $\epsilon_F$ . This pressure behavior is characteristic of metals with the electron-type conductivity, as was documented by theoretical calculations in Ref. [34]. Calculations have also shown that the valence  $d$ -electron states of Y, Rh, and Sn have a decisive contribution

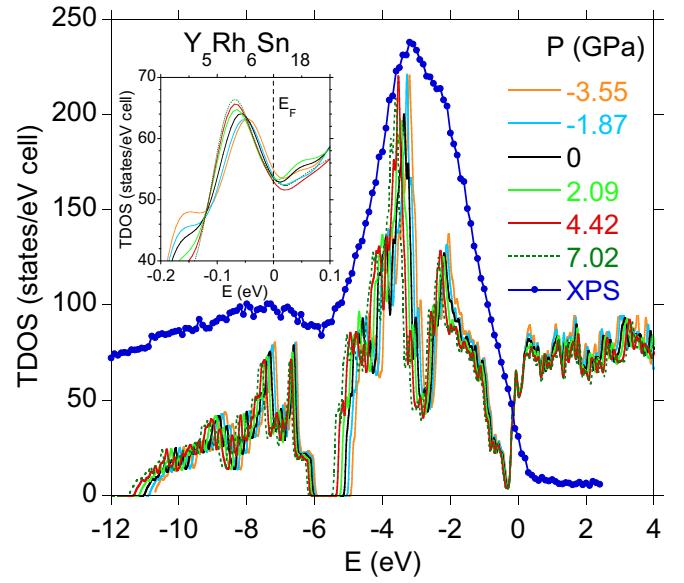


FIG. 11. The total DOS calculated for  $Y_5Rh_6Sn_{18}$  at various pressures and the VB XPS spectra measured at ambient pressure. The inset exhibits DOS details near the Fermi level.

to the total DOS at the Fermi level. The pressure effect on DOS at  $\epsilon_F$  is therefore the most noticeable for those  $d$ -electron states. Figure 12 shows the strongest pressure effect for Rh  $d$ -electron states, while for Y and Sn components the change in DOS at  $\epsilon_F$  is negligible.

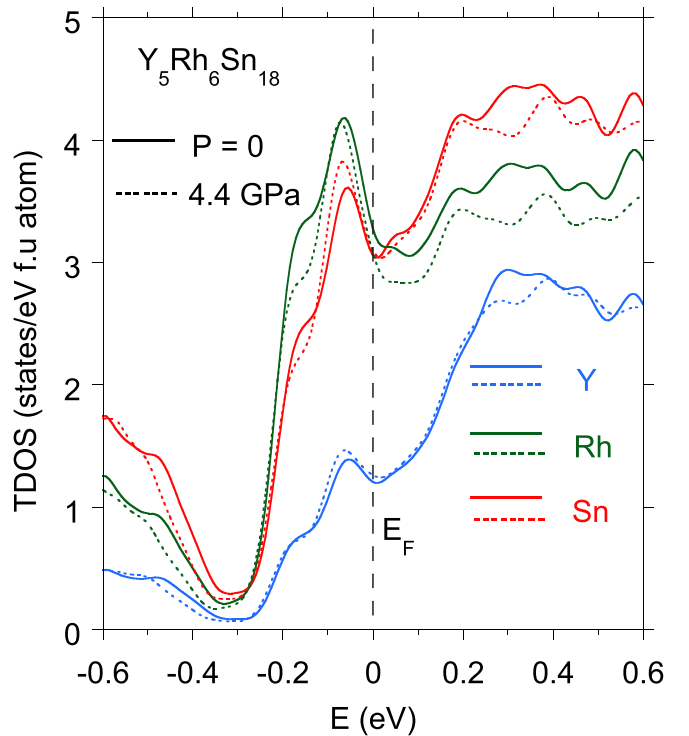


FIG. 12. The total DOS/atom near the Fermi level, calculated for  $Y_5Rh_6Sn_{18}$  at ambient pressure and for  $P = 4.4$  GPa. The solid lines represent the partial DOSs at ambient pressure, and the dotted lines represent the partial DOSs at  $P = 4.4$  GPa.



The problem of calculating  $T_c$  has been approached by McMillan [35,36] from a semiempirical point of view. Within the Eliashberg theory for strong-coupling superconductors [37], McMillan showed that a wide range of metals and alloys obey the approximate relationship

$$T_c = \frac{\theta_D}{1.45} \exp \left\{ \frac{-1.04(1 + \lambda)}{\lambda - \mu^*(1 + 0.62\lambda)} \right\}, \quad (7)$$

where  $\mu^*$  is the Coulomb pseudopotential of Morel and Anderson [38],

$$\mu^* = \frac{N(\epsilon_F)U}{1 + N(\epsilon_F)U \ln(E_B/\omega_0)}, \quad (8)$$

and the electron-phonon coupling parameter [35,39]

$$\lambda = \frac{N(\epsilon_F)\langle I^2 \rangle}{M\langle \omega^2 \rangle}. \quad (9)$$

$\langle I^2 \rangle$  is the square of the electronic matrix element of electron-phonon interactions averaged over the Fermi surface,  $\langle \omega^2 \rangle$  is an average of the square of the phonon frequency ( $\langle \omega \rangle \sim \theta_D/1.2$ ),  $N(\epsilon_F)$  is a density of states at the Fermi energy in states per electronvolt and per spin,  $M$  is the atomic mass,  $E_B$  is the electronic bandwidth, and  $\omega_0$  is the maximum phonon frequency ( $\omega_0 > \theta_D$ ). According to the BCS theory of superconductivity, a relation between  $T_c$ ,  $\langle \omega \rangle$ , and the interaction strength  $N(\epsilon_F)U$  is the following:

$$T_c = 1.14\langle \omega \rangle \exp[-1/(N(\epsilon_F)U)]. \quad (10)$$

The equivalent of  $N(\epsilon_F)U$  is approximately [40]

$$N(\epsilon_F)U \rightarrow \frac{\lambda - \mu^*}{1 + \lambda}. \quad (11)$$

By combining Eqs. (8) and (11), one is able to determine

$$N(\epsilon_F)U = \frac{-[2 + \lambda(1 - x)] + [\lambda^2(1 + x)^2 + 4\lambda + 4]^{1/2}}{2x(1 + \lambda)}, \quad (12)$$

where  $x = \ln(E_B/\omega_0)$ . For  $\text{Y}_5\text{Rh}_6\text{Sn}_{18}$   $T_c = 3.08$  K,  $T_c^* = 3.19$  K,  $\theta_D = 200$  K, and  $E_B = 4$  eV [16], then Eq. (12) allows one to estimate  $N(\epsilon_F)U = 0.2425$  for the  $T_c$  bulk phase, and  $[N(\epsilon_F)U]^* = 0.2447$  for the inhomogeneous  $T_c^*$  phase, respectively. From Eq. (12) one can also calculate  $N(\epsilon_F)U$  as a function of  $\lambda$  for the both  $T_c$  and  $T_c^*$  phases and compare them with the respective experimental values of  $N(\epsilon_F)U$ . Such a self-consistent action gives the best agreement between calculated and experimentally obtained  $N(\epsilon_F)U$  for  $\lambda = 0.46$  in the case of the bulk  $T_c$  phase and for  $\lambda^* = 0.47$  for the *disordered* phase  $T_c^*$ . The parameters  $\lambda$  and  $\lambda^*$  are very similar, which suggests that  $\text{Y}_5\text{Rh}_6\text{Sn}_{18}$  is largely homogeneous with possible intersite and/or on-site displacive atomic disorder. This is, however, not the case for the series of similar  $\text{La}_3\text{Rh}_4\text{Sn}_{13}$ ,  $\text{La}_3\text{Ru}_4\text{Sn}_{13}$ , and  $\text{Ca}_3\text{Rh}_4\text{Sn}_{13}$  superconductors, where  $\Delta\lambda$  is even of about 0.1 [13,17,31,41]. The variations of  $\lambda$  versus  $\mu^*$  shown in Fig. 13 are calculated from Eq. (7) for the  $T_c$  and  $T_c^*$  phases of  $\text{Y}_5\text{Rh}_6\text{Sn}_{18}$ . The  $\lambda(\mu^*)$  relation shown in Fig. 13 predicts for  $\mu^* = 0.1$  a value of  $\lambda$  10% larger with respect to that calculated self-consistently on the basis of Eq. (12); however, it gives identical relations between  $\lambda$  and  $\lambda^*$ . As can be seen, (i)  $\lambda$  and  $\lambda^*$  are very similar for the considered range of  $\mu^*$ ; however, always  $\lambda^* > \lambda$ . This behavior

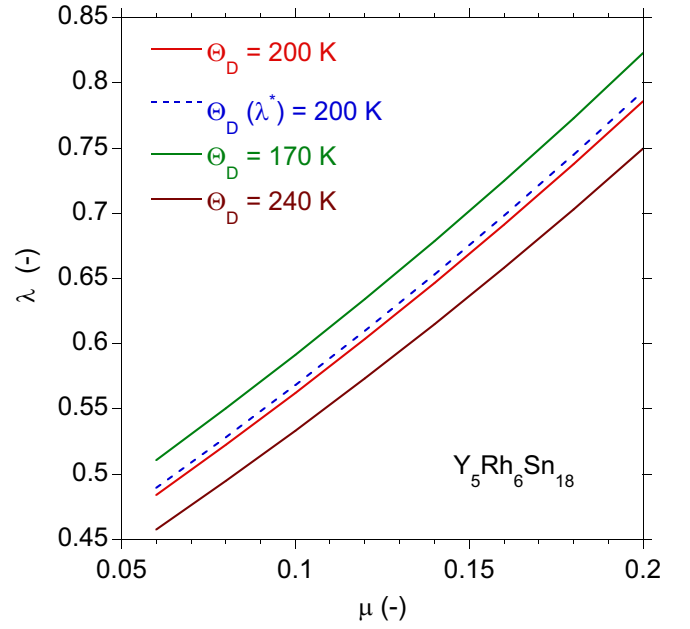


FIG. 13. Relation between electron-phonon  $\lambda$  and Coulomb repulsion coupling  $\mu^*$  parameters calculated for different Debye temperatures  $\theta_D$ . For the measured  $\theta_D = 200$  K of  $\text{Y}_5\text{Rh}_6\text{Sn}_{18}$  the dotted line (blue) represents the data for the *high-temperature*  $T_c^*$  inhomogeneous phase, while the red line displays the data for the bulk  $T_c$  phase. For  $\text{Y}_5\text{Rh}_6\text{Sn}_{18}$   $T_c^* - T_c \sim 0.1$  K. The figure also exhibits the calculated  $\lambda(\mu^*)$  dependencies for smaller and larger  $\theta_D$ .

can be interpreted as a result of larger lattice stiffening of the inhomogeneous superconducting phase  $T_c^*$  [13,41] with respect to the bulk phase  $T_c$ . (ii)  $\lambda$  is strongly  $\theta_D$  dependent, namely, enhancement of the Debye temperature  $\theta_D$  decreases  $\lambda$  of the superconducting sample. (iii) Since the Grüneisen parameter  $\gamma_G = -\frac{d \ln \theta_D}{d \ln V}$  determines the lattice stiffening, the primary reason for  $\lambda^* > \lambda$  is the pressure dependence of  $\theta_D$ , which leads to the relation  $|\frac{dT_c^*}{dP}| > |\frac{dT_c}{dP}|$  and contributes to the  $T_c^* > T_c$  effect. For the BCS superconductors the pressure variation of  $\mu^*$  is negligible, while  $\lambda$  decreases with increasing  $P$ . The empirical relation of Bennemann and Garland [42],

$$\mu^*(P) = \mu^*(0) \frac{2N(\epsilon_F, P)[2N(\epsilon_F, 0) + 1]}{2N(\epsilon_F, 0)[2N(\epsilon_F, P) + 1]}, \quad (13)$$

does not show any significant change of  $\mu^*$  for  $\text{Y}_5\text{Rh}_6\text{Sn}_{18}$  under external pressure, giving  $\Delta\mu^* = \mu^*(P = 7 \text{ GPa}) - \mu^*(0) < 2 \times 10^{-3}$ . In contrast, for classical BCS metals  $\lambda(P)$ s are expected to be about 10% lower in respect to the value of  $\lambda$  at  $P = 0$  in considered pressures  $P < 7$  GPa [40]. Differentiation of Eq. (10) with respect to  $V$  leads to the expression

$$\frac{d \ln [N(\epsilon_F, 0)U]}{d \ln V} \equiv \phi = \left( \frac{d \ln T_c}{d \ln V} - \frac{d \ln \theta_D}{d \ln V} \right) / \left( \ln \frac{\theta_D}{T_c} \right), \quad (14)$$

and  $\phi = (2\gamma_G - \frac{4}{3}) \frac{\lambda}{1 + \lambda} \frac{1 + \mu^*}{\lambda - \mu^*}$  [40,43]. For  $\text{Y}_5\text{Rh}_6\text{Sn}_{18}$ ,  $\phi = 5.3$ , which gives Grüneisen parameters  $\gamma_G = 3.35$  and  $\gamma_G^* = 3.40$ , for  $T_c$  and  $T_c^*$  phases, respectively. The relationship  $\gamma_G^* > \gamma_G$  shows that the inhomogeneous phase is characterized by

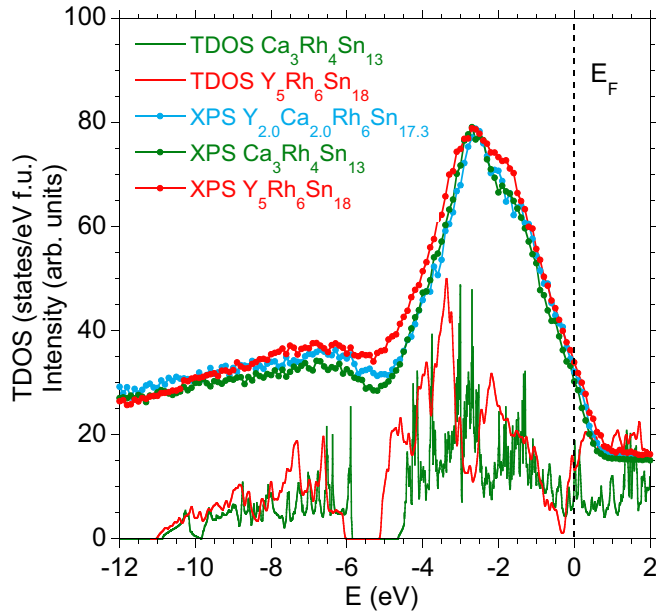


FIG. 14. VB XPS spectra for two-phase  $\text{Y}_{2.0}\text{Ca}_{2.0}\text{Rh}_{6.0}\text{Sn}_{17.3}$  sample,  $\text{Ca}_3\text{Rh}_4\text{Sn}_{13}$ , and  $\text{Y}_5\text{Rh}_6\text{Sn}_{18}$  and the calculated DOSs for the pristine samples. The spectra were normalized to the main maximum value.

greater stiffness, and while the difference in values is not large, it is, however, noticeable.

Below we analyze a strongly inhomogeneous two-phase  $\text{Y}_{5-x}\text{Ca}_x\text{Rh}_6\text{Sn}_{18}$  system  $x \sim 2$ . Microanalysis from the sample surface showed stoichiometry  $\text{Y}_{2.0}\text{Ca}_{2.0}\text{Rh}_{6.0}\text{Sn}_{17.3}$ , while XRD analysis documented 70% of a  $\text{Y}_5\text{Rh}_6\text{Sn}_{18}$ -like phase with the lattice parameters  $a = b = 13.7842 \text{ \AA}$  and  $c = 27.5037 \text{ \AA}$ , and 30% of  $\text{Ca}_3\text{Rh}_4\text{Sn}_{13}$ -like phase with  $a = 9.6915 \text{ \AA}$ , and both are inhomogeneous. Its valence-band XPS spectrum shown in Fig. 14 is in shape similar to the VB spectra of  $\text{Y}_5\text{Rh}_6\text{Sn}_{18}$  and  $\text{Ca}_3\text{Rh}_4\text{Sn}_{13}$  and lies between them, as is predicted by the calculated respective DOSs. The analysis of the  $H - T$  diagram for this dirty sample seems to be interesting for several reasons. (i) The presence of the second phases is often observed in superconducting materials. We therefore study the mechanism of enhancing the transition temperature  $T_c$  by nonmagnetic disorder and the presence of spatial inhomogeneity. (ii) The separated  $\text{Y}_5\text{Rh}_6\text{Sn}_{18}$ -like phase has almost twice larger  $T_c$  with respect to that of the parent  $\text{Y}_5\text{Rh}_6\text{Sn}_{18}$  compound [44], whereas in both cases  $H_{c2}(0)$  are similar (cf. Fig. 9). Moreover, for the dirty phase the  $H_{c2}(T)$  obtained from the specific heat data are well approximated by the WHH theory, while the resistivity data give linear  $H_{c2}(T)$  behavior and a much larger critical field  $H_{c2}(0)$  than that predicted by the WHH model [45]. (iii) As shown in Fig. 15, the pressure evolution of the electrical resistivity  $\rho(T)$  of the dirty  $\text{Y}_5\text{Rh}_6\text{Sn}_{18}$  phase can be interpreted in relation to the results from DFT calculations. Each of the measured  $\rho(T)_{P=\text{const}}$  isobars in the normal metallic state ( $T > T_c$ ) decreases its value with application of hydrostatic pressure. The  $P$  change of  $\rho$ ,  $\frac{d\rho}{dP} \cong -4.8 \mu\Omega\text{cm}/\text{GPa}$  obtained at  $T = 8 \text{ K}$  is almost the same in the whole  $T$  region. The calculated linear increase of the total DOS at  $\epsilon_F$  well correlates with that

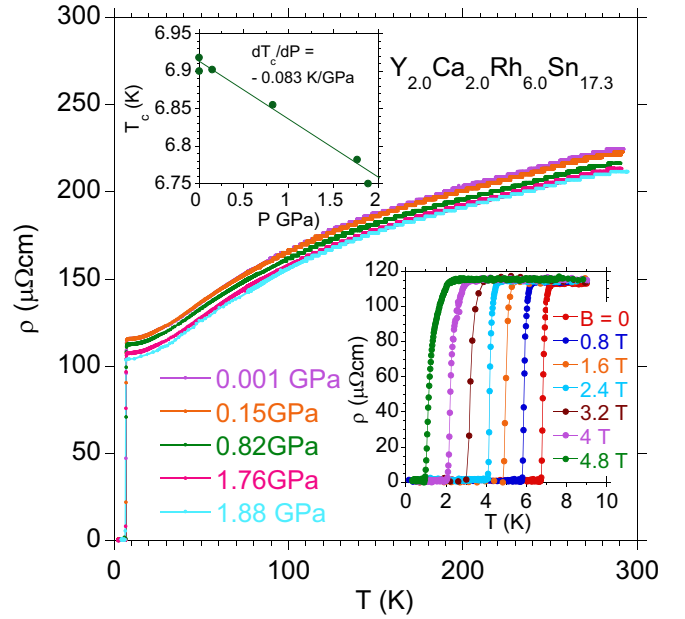


FIG. 15. Electrical resistivity for two-phase sample  $\text{Y}_{2.0}\text{Ca}_{2.0}\text{Rh}_{6.0}\text{Sn}_{17.3}$  under applied pressures. The left inset shows  $T_c^*$  vs increasing  $P$ , and the right inset displays the low-temperature electrical resistivity vs applied magnetic field.

observed for  $T > T_c$  negative  $\frac{d\rho}{dP}$  change under the assumption that  $\rho \sim 1/n$ , and the number of carriers  $n \sim \text{DOS} [n = \int \text{DOS}(E)dE]$ . No similar dependence of the resistivity on the applied magnetic field was observed. The pressure coefficient  $\frac{dT_c}{dP} = -0.09 \text{ K/GPa}$  measured for the dirty  $\text{Y}_5\text{Rh}_6\text{Sn}_{18}$  phase is similar to that of the several skutterudite-related materials [31,41]. We, however, expected about a twice larger value for this disordered phase. One of the explanations of this divergence could be the larger ionic radius of Ca with respect to Y, which results in a different effective local pressure value in the sample.

## F. Discussion

The behaviors described above fit well with the mechanism of disorder-generated  $T_c$  enhancement recently proposed by Gastiasoro and Andersen [15]. This theoretical study highlights the crucial role of spatial inhomogeneity and the generation of the local DOS enhancements due to *nonmagnetic* atomic disorder. Two scenarios are discussed for disorder-generated  $T_c$  increase: (i) dilute disorder in multiband superconductors and (ii) dense disorder in one-band superconductors. The first scenario, where the impurity resonant states generate local DOS enhancements at  $\epsilon_F$ , which can consequently raise  $T_c^*$  well above  $T_c$  of the homogeneous system, seems to qualitatively explain the increase in  $T_c$  in  $\text{Y}_5\text{Rh}_6\text{Sn}_{18}$ . In case (ii), the random disorder-generated local DOS modulations can significantly increase  $T_c$ ; this scenario describes the doped  $\text{Y}_5\text{Rh}_6\text{Sn}_{18}$  with Ca. Finally, it seems interesting to extend the present investigations of the strongly inhomogeneous systems to include the phase fluctuations effect [46].

Recently [17] for skutterudite-related compounds we documented experimentally two types of defects: Disorder caused by static displacements of atoms in cages, this is a case

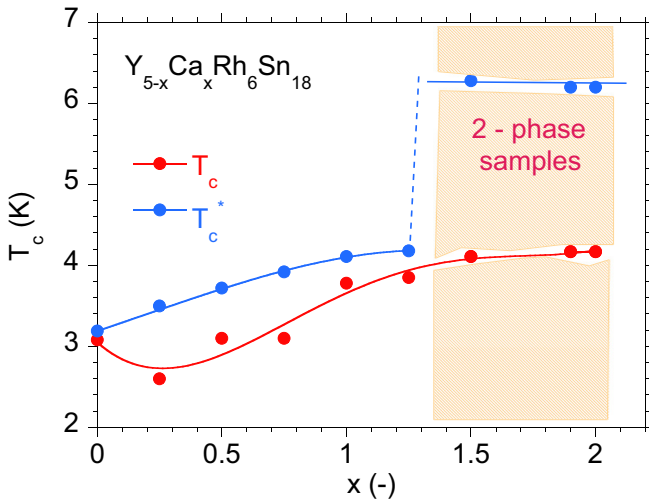


FIG. 16.  $T - x$  diagram for  $Y_{5-x}Ca_xRh_6Sn_{18}$  compounds from ac susceptibility data (see Fig. 5). For Ca content  $x > 1.25$  there are two phases: Tetragonal  $(Y:Ca)_{4.8}Rh_6Sn_{18}$ -like and cubic  $Y_{0.9}Ca_{2.1}Rh_4Sn_{13}$ -like in a volume ratio of about 80:20 (cf. Fig. 2).

of  $Y_5Rh_6Sn_{18}$ , and a disorder as a result of doping, e.g.,  $Y_5Rh_6Sn_{18}$  doped with Ca. We believe that the atomic displacements (this can also be a collective effect) contribute to the relatively small increase in  $T_c$  (observed as  $T_c^*$ ). The moderate enhancements of  $T_c$  caused by a small replacement of Y by Ca can be considered for concentration  $x \leq 1.25$ , while the doping  $x > 1.25$  is the cause of a large increase in  $T_c^*$  as a result of strong inhomogeneity. A significantly large increase in  $T_c$  is visible for two-phase samples  $x > 1.25$ , as shown in Fig. 16. One can note, however, that the boosted  $T_c$  above the concentration limit  $x \approx 1.25$  is still the effect of strong local inhomogeneity, considering that the main  $Y_5Rh_6Sn_{18}$ -type phase is formed as a nontrivial structural deformation of the cubic minority phase. Both phases have a similar ratio of respective atoms (3:4:13 and 3.33:4:12 as an effect of normalization of the number of Rh atoms to four per each formula unit), despite different crystallographic symmetries, so it can be assumed that the areas of separated phases are the areas with strong stoichiometry (homogeneity) fluctuations. This point of view is well illustrated in Fig. 17, where variations in stoichiometry over the length of the sample are compared for the single- and two-phase samples. The both samples show a similar composition of nanoscale local fluctuations, which signals site disorder, while the variations in stoichiometry of larger volume fractions ( $\sim 100 \mu m$ ) are clearly visible in Fig. 17(b) for the two-phase sample. If the two-phase system  $Y_{2.0}Ca_{2.0}Rh_{6.0}Sn_{17.3}$  can be understood as a system of strongly fluctuating inhomogeneities of the sample composition, then it is possible to explain a large difference between  $T_c$  and  $T_c^*$  on the basis of Gastiasoro and Andersen's [15] theoretical approach. The presence of the  $(Ca:Y)_3Rh_4Sn_{13}$  phase contributes to an increase in total DOS of the sample, and in effect it causes a boosted  $T_c$ . The calculated total DOS at  $\epsilon_F$  is 13.7 states/eV f.u., while for  $Y_5Rh_6Sn_{18}$  it is 11.8 states/eV f.u.

As noted earlier, an increase in disorder generates enhancement of lattice stiffening in the inhomogeneous phase and thus

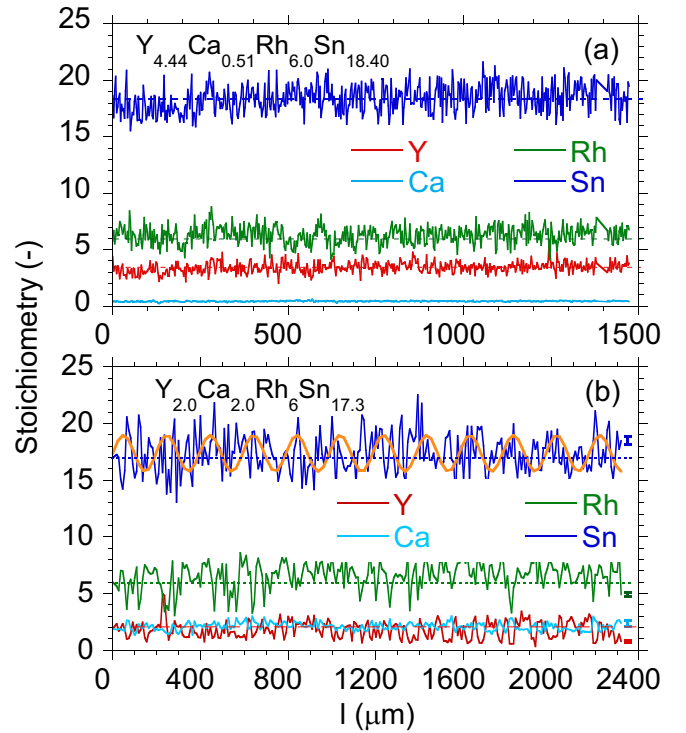


FIG. 17. Variation in stoichiometry of  $Y_{4.5}Ca_{0.5}Rh_6Sn_{18}$  (panel a) (from the EDS analysis the correct stoichiometric ratio Y:Ca:Rh:Sn was found to be  $4.44 \pm 0.15 : 0.51 \pm 0.05 : 6 \pm 0.15 : 18.5 \pm 0.4$ ) and two-phase  $Y_{2.0}Ca_{2.0}Rh_{6.0}Sn_{17.3}$  (panel b) over the length of the samples. The experimentally obtained composition by the electron microprobe technique from the total surface of each sample was closed to assumed one. The yellow curve (panel b) is a rough approximation of the fluctuating Sn around the mean content of 17.35 by the  $\sin(\frac{2\pi}{\Delta l}l)$  function with amplitude 1.6 and  $\Delta l = 21 \mu m$ , where  $\Delta l$  could express a diameter of the extent of strong fluctuations in composition.

an increase in  $T_c^*$ . To prove the correctness of this hypothesis, we calculated  $\lambda$  and  $\lambda^*$  for the system of  $Y_{1-x}Ca_xRh_6Sn_{18}$  alloys using Eqs. (10) and (12). Self-consistent calculations give for single-phase alloys  $0 < x \leq 1.25$  similar  $\lambda$  and  $\lambda^*$ , slightly larger than those obtained for pristine  $Y_5Rh_6Sn_{18}$ , as shown in Table I. Experimental data for  $T_c$ ,  $T_c^*$ , and  $\theta_D$  from low-temperature specific heat  $C/T$  approximated vs  $T^2$  to  $T^2 = 0$  were used for each alloy to determine the proper  $\lambda$  values. In contrast, for two-phase systems  $\lambda^*$ s were significantly larger, e.g., for  $Y_{2.0}Ca_{2.0}Rh_{6.0}Sn_{17.3}$   $\lambda = 0.49$ , while  $\lambda^* = 0.55$ . This behavior determines the larger stiffening of strongly inhomogeneous samples and gives a reason for strong enhancement of  $T_c^*$ .

Finally, we show the band structure of  $Y_5Rh_6Sn_{18}$  near the Fermi level in the presence of applied pressure. Its crystallographic symmetry belongs to a special class of nonsymmorphic materials. The characteristic property of band structure of such materials could be the presence of Dirac cones and Dirac nodes [47]. Our recent *ab initio* investigations carried out for the situation  $P = 0$  [16] depicted that both the character of the band structure and the shape of the Fermi surface can be linked to the occurrence of charge density waves in  $Y_5Rh_6Sn_{18}$ . Moreover, its bands revealed the presence of

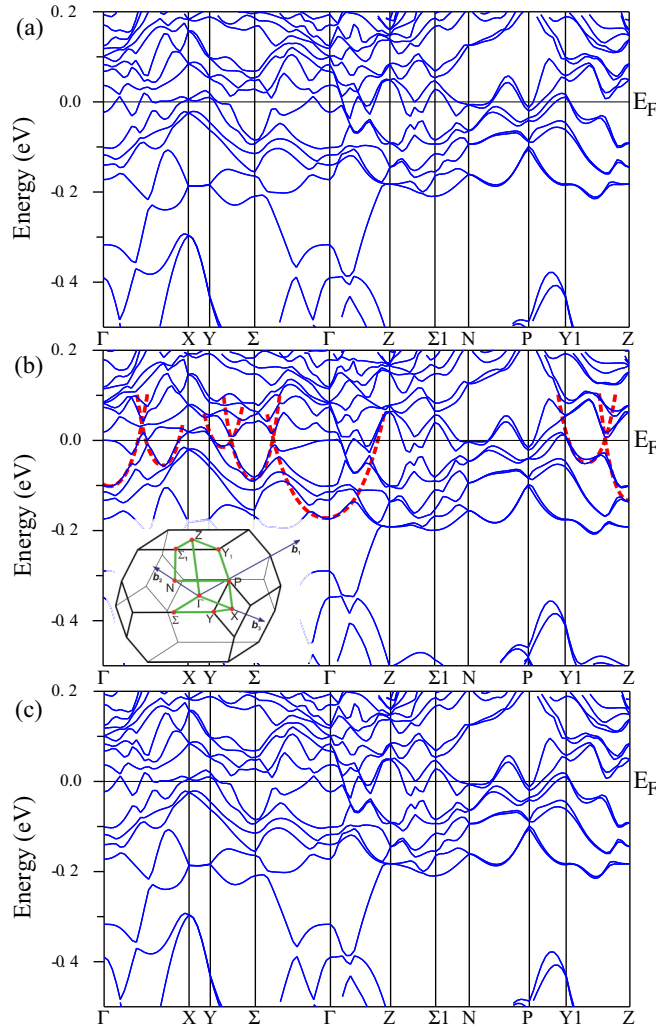


FIG. 18. Calculated band structure of  $Y_5Rh_6Sn_{18}$  for  $\Delta V/V = -0.04 \equiv P = 4.42$  GPa (a),  $\Delta V/V = 0$  at ambient pressure (b), and  $\Delta V/V = +0.04 \equiv P = -3.55$  GPa (c) along high-symmetry lines in the Brillouin zone, shown in the inset to the middle panel. Green lines depict the path used for the band structure plot. The intersections of red parabola at the Fermi level (along  $Y-\Sigma-\Gamma$  and  $Y1-Z$  lines) show electron state dispersion relations similar to a Dirac cone for the bands calculated for the state  $P = 0$ .

several Dirac cone-like shapes on  $\Gamma-Z-\Sigma-N$  symmetry lines. It is interesting whether this type of topology could also be present in the situation of applied pressure or as a result of appropriate doping. Figure 18 compares the bands near the Fermi level, calculated along high-symmetry  $k$  lines in the Brillouin zone under applied pressures  $P = 4.42$  GPa ( $\Delta V/V = -0.04$ ),  $P = 0$ , and  $P = -3.55$  GPa ( $\Delta V/V = +0.04$ ), respectively. While for  $P = 0$  the bands reveal the presence of several Dirac cone-like shapes, they can still be recognizable in applied external or chemical pressure along the high-symmetry  $k$  directions  $\Gamma-\Sigma$ ,  $\Gamma-X$ , and  $\Sigma-Y$ .

#### IV. CONCLUDING REMARKS

In this paper we discussed two main threads: The main one concerning enhancing the superconductivity of  $Y_5Rh_6Sn_{18}$

by doping with Ca, the other one the structural distortion of  $Y_5Rh_6Sn_{18}$  as a result of doping. Most of the filled skutterudite-related  $R_3M_4Sn_{13}$ -type superconductors, known as Remeika phases [48], crystallize in the cubic structure  $Pm\bar{3}n$ . Moreover, for a series of  $R_3M_4Sn_{13}$  it was claimed that the cubic crystallographic structure is modulated below temperature  $T^* \sim 130-170$  K with a  $k$ -star of a propagation vector  $\mathbf{q} = (\frac{1}{2}, \frac{1}{2}, 0)$ . The structural second order-type transition converts the simple cubic high-temperature structure  $Pm\bar{3}n$  into a body-centered cubic structure  $I4_132$  [49] with twice the lattice parameters due to the distortion of the  $Sn1Sn_{12}$  icosahedra related to a charge transfer from Sn2 toward Sn1 atoms. The structural transition temperature  $T^*$  can be suppressed to 0 K at a novel structural quantum critical point (QCP) via a suitable combination of hydrostatic pressure and chemical substitution, as was documented for  $(Sr, Ca)_3Ir_4Sn_{13}$  [50],  $(Sr, Ca)_3Rh_4Sn_{13}$  [51], or  $Ca_3(Ir, Co)_4Sn_{13}$  [52].

The cubic symmetry, however, does not support  $R = Y$  or Er. For these  $R$  atoms the tetragonal structure  $I4_1/acd$  is known. It seems that  $Y_5Rh_6Sn_{18}$  is at the border of structural stability. The lack of structural stability was a reason to investigate  $Y_5Rh_6Sn_{18}$  when Y is partially replaced by larger Ca. For the 0.25–0.50 Ca range we observed the tetragonal cell symmetry of the system, while for  $x \geq 0.75$  the main phase is no longer tetragonal. The initial analysis indicates that the deformation is most likely monoclinic. Microanalysis has confirmed that compositions with  $x < 1.5$  show inhomogeneity on an atomic scale as a result of atomic phase separation. The  $Y_{5-x}Ca_xRh_6Sn_{18}$  alloys with higher than  $x = 1.5$  Ca content have about 80% of the phase derived from a 5:6:18 system and a secondary cubic 3:4:13 cubic phase. In terms of stoichiometry, we treat the minority 3:4:13 phase as a strong homogeneity fluctuation within the bulk 5:6:18 phase (both stoichiometries are similar when normalized to Rh content). So atomic disorder has a significant impact on the physical properties of the system, especially those expressed in the case of skutterudite-related systems.

For parent  $Y_5Rh_6Sn_{18}$  compound we observed a slight increase in  $T_c$  caused by both the atomic nanoscale disorder and the static atomic displacements. Doping of  $Y_5Rh_6Sn_{18}$  with Ca ( $x \leq 1.25$ ) causes inhomogeneity of the  $Y_{5-x}Ca_xRh_6Sn_{18}$  system and enhances temperature  $T_c$ , while the strong fluctuations of stoichiometry due to much larger doping ( $x > 1.25$ ) rapidly increase  $T_c$  to the value  $T_c^* \sim 2 \times T_c$ . The mechanism for  $x$ -dependent enhancements of the superconducting transition temperature  $T_c$  in  $Y_{5-x}Ca_xRh_6Sn_{18}$  can be explained by the theoretical approach proposed by Gastiasoro and Andersen [15], both at the nanoscale nonmagnetic atomic disorder limit (dilute disorder scenario), expected for small concentration of dopant in the multiband superconductor, as well as in the proposed second scenario of dense disorder in conventional one-band superconductors, which generates strong enhancement of  $T_c$ . The basis for the interpretation of the results presented here is the observation that the Ca substitution into  $Y_5Rh_6Sn_{18}$  increases the inhomogeneity and chemical pressure in the  $Y_{5-x}Ca_xRh_6Sn_{18}$  samples. We calculated a linear increase of the DOS at  $\epsilon_F$  with  $P$  which correlates well with the measured change  $d\rho/dP$ . Our analysis of the experimental data suggests a larger Grüneisen parameter  $\gamma_G$  for the inhomogeneous superconducting state with respect to

$\gamma_G$  of the bulk  $T_c$  state, which can explain the experimental observations  $T_c^* > T_c$  and  $|dT_c^*/dP| > |dT_c/dP|$ .

### ACKNOWLEDGMENTS

A.Ś. thanks the Kosciuszko Foundation (New York) for the support of his stay and high-pressure research at the Univer-

sity of California, San Diego. M.M.M. acknowledges support by the National Science Centre (Poland) under Grant No. DEC-2018/29/B/ST3/01892. O.P. is supported by the Foundation for Polish Science (FNP), program START 66.2020. High-pressure research at the University of California, San Diego, was in part supported by NSF Grant No. DMR-1810310 and US DOE Grant No. DE-FG02-04ER46105.

- [1] For dirty superconductors a significant dependence of the pair-breaking strength on the symmetry of the scattering potential disturbed by the impurities is documented experimentally and explained theoretically.
- [2] B. T. Matthias, H. Suhl, and E. Corenzwit, *Phys. Rev. Lett.* **1**, 92 (1958).
- [3] G. Chanin, E. A. Lynton, and B. Serin, *Phys. Rev.* **114**, 719 (1959).
- [4] H. Suhl and B. T. Matthias, *Phys. Rev.* **114**, 977 (1959).
- [5] P. W. Anderson, *J. Phys. Chem. Solids* **11**, 26 (1959).
- [6] F. Steglich, J. Aarts, C. D. Bredl, W. Lieke, D. Meschede, W. Franz, and H. Schäfer, *Phys. Rev. Lett.* **43**, 1892 (1979).
- [7] N. D. Mathur, F. M. Grosche, S. R. Julian, I. R. Walker, D. M. Freye, R. K. W. Haselwimmer, and G. G. Lonzarich, *Nature (London)* **394**, 39 (1998).
- [8] M. B. Maple, P.-C. Ho, V. S. Zapf, N. A. Frederick, E. D. Bauer, W. M. Yuhasz, F. M. Woodward, and J. W. Lynn, *J. Phys. Soc. Jpn. Suppl.* **71**, 23 (2002).
- [9] R. Vollmer, A. Faißt, C. Pfleiderer, H. v. Löhneysen, E. D. Bauer, P.-C. Ho, V. Zapf, and M. B. Maple, *Phys. Rev. Lett.* **90**, 057001 (2003).
- [10] G. Seyfarth, J. P. Brison, M.-A. Méasson, D. Braithwaite, G. Lapertot, and J. Flouquet, *Phys. Rev. Lett.* **97**, 236403 (2006).
- [11] M.-A. Méasson, D. Braithwaite, G. Lapertot, J.-P. Brison, J. Flouquet, P. Bordet, H. Sugawara, and P. C. Canfield, *Phys. Rev. B* **77**, 134517 (2008).
- [12] A. Bianchi, R. Movshovich, M. Jaime, J. D. Thompson, P. G. Pagliuso, and J. L. Sarrao, *Phys. Rev. B* **64**, 220504(R) (2001).
- [13] A. Ślebarski, M. Fijałkowski, M. M. Maška, M. Mierzejewski, B. D. White, and M. B. Maple, *Phys. Rev. B* **89**, 125111 (2014).
- [14] M. Leroux, V. Mishra, J. P. C. Ruff, H. Claus, M. P. Smylie, Ch. Opagiste, P. Rodiere, A. Kayani, G. D. Gu, J. M. Tranquada, W.-K. Kwok, Z. Islam, and U. Welp, *Proc. Natl. Acad. Sci. USA* **116**, 10691 (2019).
- [15] M. N. Gastiasoro and B. M. Andersen, *Phys. Rev. B* **98**, 184510 (2018).
- [16] A. Ślebarski, P. Zajdel, M. M. Maška, J. Deniszczuk, and M. Fijałkowski, *J. Alloy. Comp.* **819**, 152959 (2020).
- [17] A. Ślebarski, P. Zajdel, M. Fijałkowski, M. M. Maška, P. Witas, J. Goraus, Y. Fang, D. C. Arnold, and M. B. Maple, *New J. Phys.* **20**, 103020 (2018).
- [18] K. Suyama, K. Iwasa, Y. Otomo, K. Tomiyasu, H. Sagayama, R. Sagayama, H. Nakao, R. Kumai, Y. Kitajima, F. Damay, J. M. Mignot, A. Yamada, T. D. Matsuda, and Y. Aoki, *Phys. Rev. B* **97**, 235138 (2018).
- [19] J. Rodriguez-Carvajal, *Physica B* **192**, 55 (1993).
- [20] ELDYF software, M. Gigla, Institute of Materials Science, University of Silesia in Katowice.
- [21] A. Ślebarski, B. D. White, M. Fijałkowski, J. Goraus, J. J. Hamlin, and M. B. Maple, *Phys. Rev. B* **86**, 205113 (2012).
- [22] P. Blaha, K. Schwarz, G. K. H. Madsen, D. Kvasnicka, J. Luitz, R. Laskowski, F. Tran, and L. D. Marks, WIEN2K, *An Augmented Plane Wave + Local Orbitals Program for Calculating Crystal Properties* (Karlheinz Schwarz, Technische Universität Wien, Austria, 2001).
- [23] D. J. Singh and L. Nordstrom, *Plane Waves, Pseudopotentials, and the LAPW Method*, 2nd ed. (Springer Science, New York, 2006).
- [24] F. D. Murnaghan, *Proc. Natl. Acad. Sci. USA* **30**, 244 (1947).
- [25] J. P. Perdew, A. Ruzsinszky, G. I. Csonka, O. A. Vydrov, G. E. Scuseria, L. A. Constantin, X. Zhou, and K. Burke, *Phys. Rev. Lett.* **100**, 136406 (2008).
- [26] The anomaly at  $T_c^*$  marks the onset of an inhomogeneous superconducting phase with spatial distribution of the magnitude of the superconducting energy gaps. Following Ref. [13], a simple Gaussian gap  $f(\Delta) \propto \exp[-\frac{(\Delta-\Delta_0)^2}{2D}]$  distribution approximates, e.g., the specific heat data obtained for temperatures  $T_c < T < T_c^*$ .  $\Delta_0$  and  $D$  are treated as fitting parameters.
- [27] E. Helfand and N. R. Werthamer, *Phys. Rev. Lett.* **13**, 686 (1964); N. R. Werthamer, E. Helfand, and P. C. Hohenberg, *Phys. Rev.* **147**, 295 (1966).
- [28] E. Helfand and N. R. Werthamer, *Phys. Rev.* **147**, 288 (1966).
- [29] P. G. De Gennes, *Phys. Condens. Mater.* **3**, 79 (1964); K. Maki, *Physics* **1**, 27 (1964); P. G. De Gennes, *Superconductivity in Metals and Alloys* (W. A. Benjamin, New York, 1966).
- [30] T. P. Orlando, E. J. McNiff, Jr., S. Foner, and M. R. Beasley, *Phys. Rev. B* **19**, 4545 (1979).
- [31] A. Ślebarski, J. Goraus, M. M. Maška, P. Witas, M. Fijałkowski, C. T. Wolowiec, Y. Fang, and M. B. Maple, *Phys. Rev. B* **93**, 245126 (2016).
- [32] J. P. Carbotte, *Rev. Mod. Phys.* **62**, 1027 (1990).
- [33] A. Gurevich, *Phys. Rev. B* **67**, 184515 (2003).
- [34] L. Hai, L. Zhengzhong, X. Mingwen, and X. Xiaohua, *Commun. Theor. Phys.* **31**, 49 (1999); S. Shang, *Phys. Rev. B* **65**, 064407 (2002).
- [35] W. L. McMillan, *Phys. Rev.* **167**, 331 (1968).
- [36] R. C. Dynes, *Solid State Commun.* **10**, 615 (1972).
- [37] G. M. Eliashberg, *Sov. Phys. JETP* **11**, 696 (1960); **12**, 1000 (1961).
- [38] P. Morel and P. W. Anderson, *Phys. Rev.* **125**, 1263 (1962).
- [39] J. J. Hopfield, *Phys. Rev.* **186**, 443 (1969).
- [40] P. E. Seiden, *Phys. Rev.* **179**, 458 (1969).
- [41] A. Ślebarski, M. M. Maška, M. Fijałkowski, C. A. McElroy, and M. B. Maple, *J. Alloy. Comp.* **646**, 866 (2015).

- [42] K. H. Bennemann and J. W. Garland, in *Superconductivity in d- and f-Band Metals*, edited by D. H. Douglass, AIP Conference Proceedings No. 4 (American Institute of Physics, New York, 1972), p. 103.
- [43] W. Wejgaard, *Phys. Lett. A* **29**, 396 (1969).
- [44] The increase in both  $T_c$  and  $H_{c2}(0)$  is characteristic of similar skutterudite-related systems, when they are doped [17].
- [45] For disordered superconductors the critical temperature  $T_c^*$  obtained from the resistivity  $\rho(T)$  is usually larger than this temperature obtained from the specific heat data. The specific heat shows for a strongly inhomogeneous phase weak and broad maximum, well approximated by the function  $f(\Delta)$ , and  $T_c^*$  is the temperature of maximum in  $f(\Delta)$  distribution, while  $\rho$  measures the critical temperature between the normal and superconducting states for  $T_c^*$ , where the process begins. It is worth noting that the  $H - T$  diagram for strongly inhomogeneous  $\text{Y}_{2.0}\text{Ca}_{2.0}\text{Rh}_{6.0}\text{Sn}_{17.3}$  sample shows the deviation between the data determined from  $C$  and  $\rho$  measurements, respectively, for  $T < 3.5$  K; moreover, the  $H_c(T)$  curve obtained from the specific heat data is well approximated by the WHH theory.
- [46] I. Martin, D. Podolsky, and S. A. Kivelson, *Phys. Rev. B* **72**, 060502(R) (2005).
- [47] S. M. Young and C. L. Kane, *Phys. Rev. Lett.* **115**, 126803 (2015).
- [48] J. P. Remeika, G. P. Espinosa, A. S. Cooper, H. Barz, J. M. Rowel, D. B. McWhan, J. M. Vandenberg, D. E. Moncton, Z. Fizek, L. D. Woolf, H. C. Hamaker, M. B. Maple, G. Shirane, and W. Thomlinson, *Solid State Commun.* **34**, 923 (1980); J. L. Hodeau, M. Marezio, J. P. Remeika, and C. H. Chen, *ibid.* **42**, 97 (1982).
- [49] P. Bordet, D. E. Cox, G. P. Espinosa, J. L. Hodeau, and M. Marezio, *Solid State Commun.* **78**, 359 (1991).
- [50] L. E. Klintberg, S. K. Goh, P. L. Alireza, P. J. Saines, D. A. Tompsett, P. W. Logg, J. Yang, B. Chen, K. Yoshimura, and F. M. Grosche, *Phys. Rev. Lett.* **109**, 237008 (2012).
- [51] S. K. Goh, D. A. Tompsett, P. J. Saines, H. C. Chang, T. Matsumoto, M. Imai, K. Yoshimura, and F. M. Grosche, *Phys. Rev. Lett.* **114**, 097002 (2015).
- [52] J. Hou, C. H. Wong, R. Lortz, R. Sibille, and M. Kenzelmann, *Phys. Rev. B* **93**, 134505 (2016).